Nano Research

ISSN 1998-0124 CN 11-5974/O4
https://doi.org/10.1007/s12274-022-4215-8

Research Article

Dehydro-Diels–Alder reaction and diamondization of bowl-shaped clusters $C_{18}Te_3Br_4(Bu\text{-}O)_6$

Jinbo Zhang[1,2], Manli Ma[1], Rong Zhou[1], Hongqiang Chu[1], Xue Wang[1], Shaojie Wang[2], Huhu Tian[3,4], Zhipeng Yan[5], Mingtao Li[6], Zhongyan Wu[7], Bin Li[7], Jiafeng Yan[7], Lan Anh Thi Nguyen[7], Rongxing Cao[1], Guoqing Wu[1], Xianghua Zeng[1], Hao-Li Zhang[3] (✉), Jaeyong Kim[7] (✉), Lin Wang[2] (✉), and Yongjun Tian[2]

[1] *College of Physical Science and Technology, Yangzhou University, Yangzhou 225002, China*
[2] *Center for High Pressure Science (CHiPS), State Key Laboratory of Metastable Materials Science and Technology, Yanshan University, Qinhuangdao 066004, China*
[3] *State Key Laboratory of Applied Organic Chemistry, Lanzhou University, Lanzhou 730000, China*
[4] *Baotou Research Institute of Rare Earths, Baotou 014000, China*
[5] *Academy for Advanced Interdisciplinary Studies, Southern University of Science and Technology, Shenzhen 518055, China*
[6] *Center for High Pressure Science and Technology Advanced Research, Shanghai 201203, China*
[7] *Department of Physics, and High Pressure Research Center, Hanyang University, Seoul 04763, Republic of Korea*

Received: 29 December 2021 / **Revised:** 5 February 2022 / **Accepted:** 7 February 2022

ABSTRACT

Dehydro-Diels–Alder (DDA) reaction is a textbook reaction for preparing six-membered rings in solution but is scarcely seen in solid-state synthesis. In this work, using multiple characterization techniques, we demonstrate that the bowl-shaped clusters $C_{18}Te_3Br_4(Bu\text{-}O)_6$ might experience a DDA reaction at room temperature and high pressure between 5.5 and 7.4 GPa. Above 17.0 GPa, it is found that the bonding conversion from the intramolecular sp^2 to the intermolecular sp^3 occurred, in the form of pressure-induced diamondization. The recovered samples from 20.0 and 36.1 GPa showed incomplete reversibility, while the decompression-induced graphitization of glassy carbon was observed during decompression from 46.5 GPa. The electrochemical impedance spectroscopy results indicated that the transport properties changed from grain boundary dominant to grain dominant due to the DDA reaction and the grain boundary effect disappeared as the intermolecular sp^3 bonding building-up and carrier transmission channel formation above 17.0 GPa. The results in this study open a new route to construct the crystalline carbon materials with different transport properties.

KEYWORDS

polycyclic aromatic hydrocarbons, dehydro-Diels–Alder reaction, diamondization, high-pressure

1 Introduction

Organic molecular crystals are a class of soft and easily compressible solids. The combination of weak intermolecular forces and strong intramolecular covalent bonds results in organic molecular crystals with unique properties. For example, flexible organic photoelectric functional materials have been created [1, 2]. High-pressure is an important thermodynamic method for tuning the properties of crystal structures [3–5]. Under high-pressure conditions, the intermolecular distances will change significantly, reorganizing crystal packing and changing the properties of the material [6–12], and many examples of pressure-induced phase transitions or polymerization of organic molecules have been reported. Benzene presents several structural changes at pressures of 1.4, 4, 11, and 17 GPa, and exposing benzene to pressures in excess of 25 GPa results in irreversible chemical reaction, creating amorphous hydrogenated carbons (a-C:H) [10, 13]. A semimetal-to-semiconductor transition of trilayer graphene was obtained by tuning the interlayer interactions with pressure, achieving an intrinsic bandgap of 2.5 ± 0.3 eV, and the high-pressure semiconducting phase was preserved even at several GPa [11]. Researchers have examined C_6H_6–C_6F_6 co-crystals under high-pressure conditions and found that they polymerized into layered H–F graphene after several elemental reactions [14, 15]. Furthermore, some polycyclic aromatic hydrocarbons (PAHs), such as naphthalene, anthracene, and pentacene, will convert to graphite or diamond under extreme conditions, and pentacene exhibits metallic properties at 27 GPa [16, 17]. Unlike widely studied flat PAHs, few studies examined curved PAHs under high-pressure conditions. Curved PAHs, also classified as fullerenes, exhibit unique physical and chemical properties due to their unique concave-convex structure. Many studies have been conducted on closed systems of fullerenes at high-pressures such as C_{60} [18–20], C_{70} [21], and carbon nanotubes [22]. However, curved PAHs, such as bowl-shaped molecules, have an open surface and exhibit unique properties. As a result, they can be used in areas such as synthetic chemistry and photoelectric materials due to their geometric configurations and molecular dipoles [23, 24]. Raman and infrared (IR) absorption spectra of bowl-shaped corannulene have been studied up to 27.6 GPa, and

Address correspondence to Hao-Li Zhang, haoli.zhang@lzu.edu.cn; Jaeyong Kim, kimjy@hanyang.ac.kr; Lin Wang, linwang@ysu.edu.cn

two phase transitions were observed at 2.2 and 3.6 GPa, while at 11.4 GPa, corannulene began to polymerize irreversibly. Upon loading pressure to 19.7 GPa, corannulene then transformed into amorphous hydrocarbon with mixed sp^2 and sp^3 bonding [25–27]. Recently, Liu et al. and Gou et al. synthesized millimetre-sized, nearly pure sp^3 amorphous carbon material at 27 GPa and 900–1,000 K, and paracrystalline diamond at 30 GPa and 1,600 K, respectively from C_{60} precursors [28, 29].

Trichalgenasumanenes synthesized through the substitution of pentagonal carbon by heteroatoms (S, Se, and Te) are good example of organic molecules with bowl-shaped structures and narrow highest occupied molecular orbital (HOMO)–lowest unoccupied molecular orbital (LUMO) gaps, compared with sumanenes [30, 31]. In addition, the tellurium atoms in the pentagon structures will coordinate with bromine, resulting in obvious physical and chemical property changes [32]. Compared to trithiasumanene with a bowl depth ~ 0.65 Å and triselenasumanene with a bowl depth ~ 0.47 Å, $C_{18}Te_3Br_4$(Bu-O)$_6$ has a bowl-shaped polycyclic skeleton with a shallow bowl depth, resulting in a molecular skeleton that is almost planar, as shown in Fig. 1. In addition, the evolution of transport behavior and structure of $C_{18}Te_3Br_4$(Bu-O)$_6$ under pressure have not yet been explored.

In this study, we investigated bowl-shaped $C_{18}Te_3Br_4$(Bu-O)$_6$ under high-pressure and room temperature conditions. The transport properties were analyzed along with structural changes according to IR absorption and Raman spectroscopy and synchrotron X-ray diffraction (XRD) analysis, and our results demonstrated the evident effects of pressure on the structure of $C_{18}Te_3Br_4$(Bu-O)$_6$.

2 Experimental section

Polycrystalline powder $C_{18}Te_3Br_4$(Bu-O)$_6$ sample was synthesized from hexaalkoxytriphenylene using an ultrasound-assisted one-pot reaction [31]. An *in situ* high-pressure study on $C_{18}Te_3Br_4$(Bu-O)$_6$ was then performed using symmetric diamond anvil cell with Fe gaskets, and ruby fluorescence line-shift was employed for pressure calibration [33]. The transport behavior of $C_{18}Te_3Br_4$(Bu-O)$_6$ was measured using electrochemical impedance spectroscopy (Solartron-1296 & 1260), where the alternating current (AC) voltage was 100 mV and the frequency ranged from 0.01 Hz to 10 MHz. A mixture of epoxy and cubic boron nitride (c-BN) was used as the insulation between the electrode and the Fe gasket. Two thin platinum electrodes were then connected to the sample, and no pressure medium was used for high-pressure electrochemical impedance spectroscopy measurements [34]. IR spectra were obtained using a Bruker VERTEX 70v Fourier transform infrared spectrometer, and the data were collected in transmission mode with a resolution of 0.4 cm^{-1}. The sample chamber was filled with a mixture of sample and potassium bromide (KBr). Raman data were collected using a Renishaw micro-Raman spectrometer, and the system utilized an Nd:YAG laser instrument operating at 532 nm with a spectral resolution of better than 1 cm^{-1}. The synchrotron XRD study on $C_{18}Te_3Br_4$(Bu-O)$_6$ under high-pressure was performed at the Pohang Accelerator Laboratory on a beamline 5A. The wavelength of the incident X-ray was 0.6927 Å, and two-dimensional data images were integrated using Dioptas software [35]. Silicone oil was used as the pressure transmitting medium in the high-pressure Raman and XRD experiments.

3 Results and discussion

We obtained the IR absorption spectra of $C_{18}Te_3Br_4$(Bu-O)$_6$ at room temperature and at pressures ranging from ambient pressure to 36.1 GPa. The region from 940 to 1,360 cm^{-1} corresponded to C–O and C–C stretching vibrations, as well as the stretching and angular vibrations of $–CH_3$ and $–CH_2–$ in the fingerprint region. The 1,430–1,660 cm^{-1} region included $–CH_3$ and $–CH_2–$ angular vibrations and carbon–carbon (sp^2) stretching of the carbon ring, and the 2,870–2,960 cm^{-1} band was assigned to the stretching of C(sp^3)–H. The internal stress due to the incorporation of pentagons in the curved PAHs produced a blue shift in the vibration frequency; however, this effect was negligible in the bowl-shaped PAHs with shallow bowl depth [30]. Besides, the vibration frequency presented red shift in heteroatom-bearing five membered ring compared to pentagonal carbon ring in other organic materials due to the substitution of C atom in the pentagon by heavier Te atom.

A few selected IR spectra are shown in Fig. 2. During compression up to 7.4 GPa, the C–H stretching vibrations (sp^3 $\upsilon_{(C-H)}$) in the ~ 2,850–2,990 cm^{-1} region from the sp^3 carbon in the butyl group ($–CH_2–CH_2–CH_2–CH_3$) broadened and weakened, and one absorption peak at 1,360 cm^{-1} marked by blue triangle of the C–H in-plane vibrations (sp^3 $\beta_{(C-H)}$) weakened rapidly. We also observed a shoulder at 3,035 cm^{-1} and a peak at 3,107 cm^{-1}, which were attributed to the C–H stretching vibrations of the sp^2 carbon in the 3-butenyl group ($–CH_2–CH_2–CH=CH_2$), and their intensities increased with increasing pressure. These changes indicated that $C_{18}Te_3Br_4$(Bu-O)$_6$ might experience a pressure-induced dehydro-Diels–Alder (DDA) reaction, namely decomposition, in which the saturated carbon atoms (sp^3-type) decomposed into unsaturated carbon atoms (sp^2-type) [36–42]. After decomposition of $–CH_2–CH_2–CH_2–CH_3$ into $–CH_2–CH_2–CH=CH_2$, the resulting products consisted of hydrogen and $C_{18}Te_3Br_4$(3-butenyl-O)$_6$. When the pressure was further increased to 22.5 GPa, the peak at 1,300 cm^{-1} attributed to the $\upsilon_{(C-C)}$ in carbon rings and the peak at 3,035 cm^{-1} belonging to the C–H stretching vibrations of the sp^2 carbon disappeared,

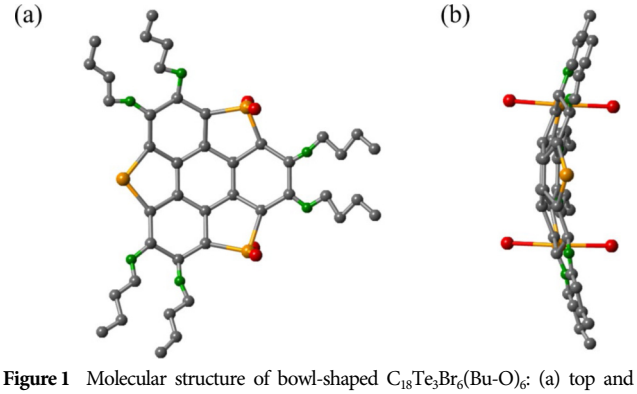

Figure 1 Molecular structure of bowl-shaped $C_{18}Te_3Br_6$(Bu-O)$_6$: (a) top and (b) side views.

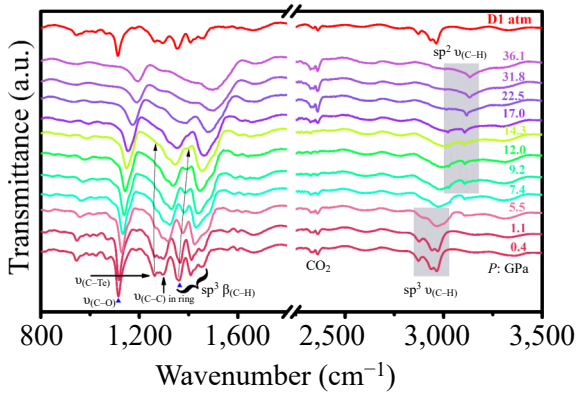

Figure 2 Selected IR spectra of $C_{18}Te_3Br_4$(Bu-O)$_6$.

indicating the decrease of intramolecular sp^2 bonding.

IR absorption spectra of the recovered sample from 36.1 GPa had the same profile as the original sample. However, the absorption peak intensity was lower than before loading pressure was applied, and as a result, reversibility was incomplete.

Raman spectroscopy is the most effective and non-destructive method for characterizing the free carbon phase. Figure 3(a) shows the Raman spectra of $C_{18}Te_3Br_4(Bu\text{-}O)_6$ up to 46.5 GPa. After 6.7 GPa, the strong peak at 174 cm^{-1} developed into a broad and weak hump, possibly due to the pressure-induced DDA reaction. Lattice vibration signals from 130 to 220 cm^{-1} decreased with increasing pressure, indicating amorphous state forming. Above 24.0 GPa in compression, the $\upsilon_{(C-C)}$ mode in ring at around 1,500 cm^{-1} and G band at ~ 1,600 cm^{-1} gradually disappeared as shown in Fig. 3(b), suggesting sp^2 bonding in a molecule converts to intermolecular sp^3 bonding [43]. During pressure release from 46.5 GPa, the G band transformed into a broad and asymmetric band, which characterized the conversion from sp^3 bonding to sp^2 bonding [44]. Figure 3(c) presents clearly the G band position and full width at half maximum (FWHM) upon loading pressure. At the pressure ranges of 6.7–11.3 and 17.5–24.0 GPa in compression, the peak position and FWHM presented two abrupt changes which correspond to DDA reaction and diamondization, respectively. The transition from van der Waals interactions between the molecules to intermolecular sp^3 bonding in amorphous carbon is also known as solid-state topochemical polymerization (SSTP) [45–47]. In addition, the D (~ 1,350 cm^{-1}) and 2D (~ 2,700 cm^{-1}) bands were also unavailable, as they overlapped with the first- and second-order Raman peaks of diamond, respectively, or they were not present.

Experimental evidences and theoretical results have shown that high sp^3 glassy carbon loaded up to 45 GPa will fully revert to oriented sp^2-bonded graphite after decompression [17, 48, 49]. Ferrari and Robertson proposed a three-stage model to classify disordered, amorphous, and diamond-like carbon using the positions, intensities, and widths of the G and D bands in the visible Raman spectra [44]. In this study, no H_2 Raman ~ 4,230 cm^{-1} signal was visible, indicating that only hydrogen atoms were presented as a result of decomposition. Thus, our results were inconsistent with the conclusions obtained by Lim et al., who used Raman spectral evidence to show that solid H_2 intercalated into graphite at pressures up to 60 GPa [50].

To elucidate the structural changes with pressure, we conducted *in situ* synchrotron XRD measurements. The selected diffraction patterns at high-pressure are shown in Fig. 4, where the weak peak intensity illustrated poor crystallinity due to weak interactions between the molecules. At 3.6 GPa, the marked peaks were indexed as the diffraction of monoclinic structure ($P2_1/c$ space group, a = 10.415 Å, b = 7.501 Å, c = 3.961 Å, and β = 118.1°). No detectable XRD pattern changes were observed in the sample between 9.7 and 20.6 GPa, corresponding to the pressure-induced DDA reaction and conversion from intramolecular sp^2 bonding to intermolecular sp^3 bonding, respectively. Therefore, the decomposition products, $C_{18}Te_3Br_4(3\text{-butenyl-}O)_6$, maintained their structural relationships with the reactants, specifically the solid-state topochemical reaction, decomposition, and polymerization. At 20.6 GPa in compression, the sample signal disappeared, indicating the transition into an amorphous structure being consistent with Raman observation. After the pressure was released at 20.6 GPa, the XRD peak at 2θ = 3.97° recovered, though the other weak peaks were not visible, indicating that the phase transition of $C_{18}Te_3Br_4(Bu\text{-}O)_6$ exhibited incomplete reversibility with a strong preferred orientation. These results were agreeable with the conclusions obtained by Shiell et al. [49]. High-pressure studies have shown that glassy carbon undergoes a reversible phase transition into super-hard amorphous diamond via continuous pressure-induced sp^2 bonding to sp^3 bonding changes at loading pressures above 40 GPa under ambient temperature conditions [51]. According to the conclusions obtained from Raman spectroscopy and XRD analysis on the layered graphene under high-pressure conditions [52] that it becomes amorphous with an interlayer distance of 2.8 Å (above 18 GPa); however, local sp^2 hybridization in the layers persisted until 50 GPa.

The Nyquist plots for different pressures are presented in Figs. 5(a)–5(d). The Nyquist plots contained three semicircles at 2.1 GPa in which the first semicircle in the high-frequency region represented the grain resistance and the second semicircle in the middle-frequency region represented the grain boundary resistance, so $C_{18}Te_3Br_4(Bu\text{-}O)_6$ presented electron transport behavior. The third semicircle in the low-frequency corresponded to the contact resistance, which was related to the surface effect between the sample and Pt electrodes [53, 54]. As the pressure increased, the low-frequency semicircle gradually disappeared, indicating good contact between the sample and the Pt electrodes. The diameters of the first two semicircles decreased with increasing pressure, indicating that the resistance decreased. Above 8.2 GPa, the diameter of the semicircle in the middle-frequency region suddenly became smaller than the semicircle in the high-frequency region, indicating that grain resistance dominated the transport behavior. Thus, the grain boundary resistance contributed less to the total resistance. From 20.2 GPa during compression, the second semicircle in the middle-frequency region disappeared, meaning grain boundary

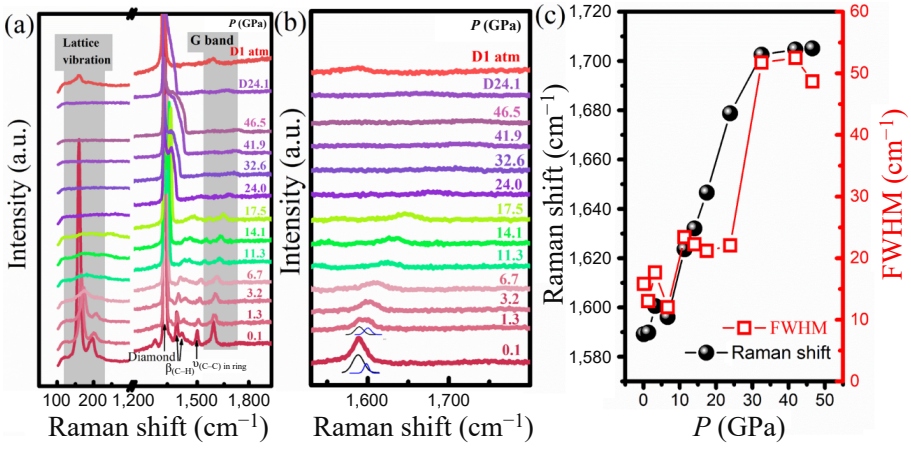

Figure 3 (a) Selected Raman spectra of $C_{18}Te_3Br_4(Bu\text{-}O)_6$. (b) Enlarged Raman spectra from 1,550 to 1,800 cm^{-1} and double peaks fit, that are graphite (1,585 cm^{-1}) and nanocrystalline graphite (1,600 cm^{-1}). (c) Pressure dependence of the G band.

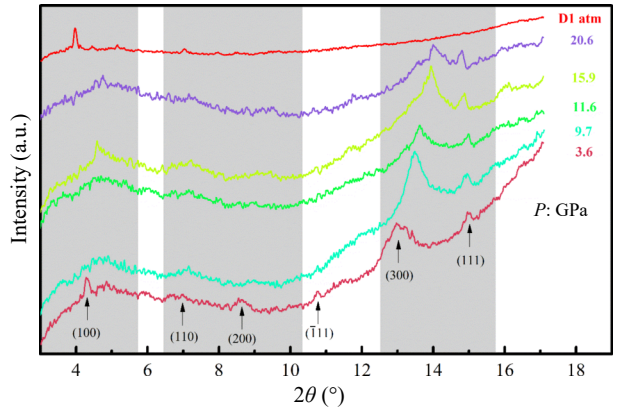

Figure 4 Selected *in situ* synchrotron XRD patterns of $C_{18}Te_3Br_4(Bu\text{-}O)_6$ under high-pressure conditions at room temperature.

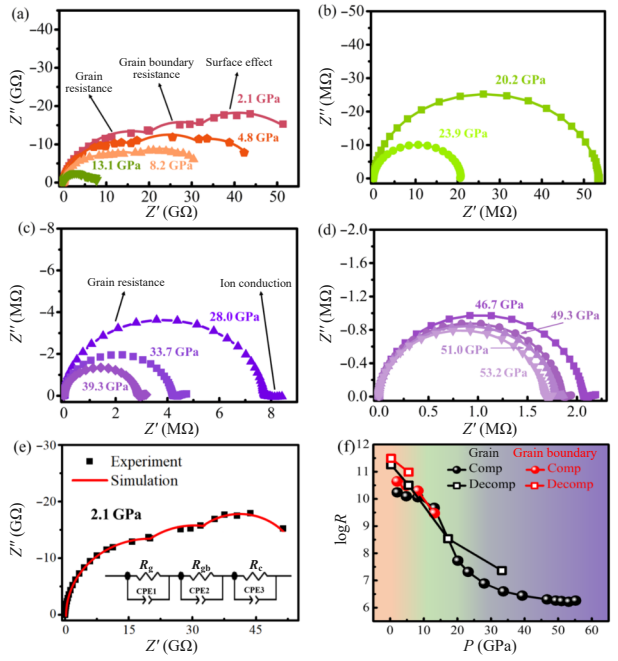

Figure 5 (a)–(d) Nyquist plots of $C_{18}Te_3Br_4(Bu\text{-}O)_6$ upon loading pressure at different pressure. (e) Equivalent circuit and fitted experimental results at 2.1 GPa, where R_g and R_{gb} represent the grain resistance and grain boundary resistance, respectively, CPE1 and CPE2 are the constant phase angle elements, R_c is the contact resistance, and CPE3 is the capacitance associated with the contact surface of the sample and electrode. (f) Evolution of grain resistance and grain boundary resistance with pressure.

disappeared and molecules polymerized under high pressure as described in Raman characterization. Above 23.9 GPa, a short straight line appeared in the low-frequency region, indicating ionic conduction. The angle between the short straight line and Z'-axis was less than 45°, possibly due to the rough surface of the electrode.

To quantify the effects of pressure on the transport properties of $C_{18}Te_3Br_4(Bu\text{-}O)_6$, an equivalent circuit model was employed to fit the electrochemical impedance spectra, as shown in the inset in Fig. 5(e). The experimental and fitted results were in good agreement. R_g was smaller than R_{gb} between 2 and 8 GPa, and above ~ 8 GPa, R_{gb} and R_g dropped rapidly, as shown in Fig. 5(f). As the pressure increased further, R_g decreased rapidly until ~ 23.9 GPa, and afterward, R_g decreased slowly until 53.2 GPa. The variations of R_{gb} and R_g from 8.2 to 13.1 GPa and above 23.9 GPa were attributed to the structural changes with pressure increasing of $C_{18}Te_3Br_4(Bu\text{-}O)_6$. After decompression, R_g and R_{gb} almost recovered to their values, indicating that the recovered samples had close relationship with virgin samples.

Carbon is a versatile element, which can crystallize in the form of cubic diamond, graphite, and amorphous carbon usually. Great excitement has followed the discovery of new forms of carbon, including fullerenes, nanotubes, and single layer graphene [55]. Functionalized carbon materials modified by ions offer broad potential applications in telecommunications, electronics, catalysis, and ion battery [56–60].

In this report, IR absorption spectroscopy analysis of $C_{18}Te_3Br_4(Bu\text{-}O)_6$ indicated that it decomposed into hydrogen and $C_{18}Te_3Br_4(3\text{-butenyl-}O)_6$ at 7.4 GPa, specifically from $-CH_2-CH_2-CH_2-CH_3$ to $-CH_2-CH_2-CH=CH_2$. According to the XRD results, some of the resulting hydrogen atoms were absorbed by the Fe gasket to low the transition pressures to 9.7 GPa from 13 GPa at ambient temperature, from body-centered cubic (bcc) Fe to hexagonal close packed (hcp) Fe (see the Electronic Supplementary Material (ESM)). The decomposition of PAHs under high-pressure was the source of hydrogen and amorphous hydrogenated carbon, and this result may be relevant for environmental applications [39, 41]. In this study, when we further increased the pressure above 17.0 GPa, $C_{18}Te_3Br_4(3\text{-butenyl-}O)_6$ converted from intramolecular sp^2 bonding in the molecular crystals to intermolecular sp^3 bonding in the amorphous carbon. Therefore, pressure-induced diamondization occurred under high-pressure, as shown in the IR absorption and Raman spectra. We also observed competition of the hydrogen atoms from the pressure-induced DDA reaction between $C_{18}Te_3Br_4(3\text{-butenyl-}O)_6$ and the Fe gasket. It is suggested that pressure-induced diamondization occurred via sp^3 bonding of the carbons in the rings (C–C bridge) and the carbons of $-CH_2-CH_2-CH=CH_2$ in 3-butenyl (on the molecular edges) from the adjacent molecules; thus, a carbon network formed with high sp^3 bonding. As a result, a good carrier (electrons and ions) transmission channel was established, which decreased resistance. After release, the IR absorption spectra recovered their profile with lower intensities compared to the highest studied pressure of 36.1 GPa, and the XRD pattern after pressure release resembled the virgin sample at the highest studied pressure of 20.6 GPa. These results indicated that incomplete reversibility occurred upon release of pressure. We proposed that decompression consisted of two stages. In the first stage, all C–C bridges were broken, however, some sp^3 bonding on the molecular edges survived, cluster consisting of two or fewer molecules formed. In the second stage, the resulting hydrogen atoms from the DDA reaction were absorbed by $C_{18}Te_3Br_4(3\text{-butenyl-}O)_6$, and as a result, $C_{18}Te_3Br_4(Bu\text{-}O)_6$ recovered. However, the Raman spectra indicated decompression-induced graphitization at 46.5 GPa; therefore, the critical pressure existed between 36.1 and 46.5 GPa, being consistent with the results obtained by Shiell et al. (45 GPa) [49]. Above the critical pressure, the conversion was irreversible, and some of C–C bridges were broken. However, all of the sp^3 bonds on the edges of the molecules remained, resulting in a carbon network composed of low sp^3 amorphous carbon. Figure 6 shows the schematic $C_{18}Te_3Br_4(Bu\text{-}O)_6$ evolution with high pressure. Research by Mao et al. revealed that graphite exposed to compression at ambient temperature experienced a transition into distorted super-hard material at 17 GPa, where half of the interlayer π-bonds in graphite converted to σ-bonds through bridging of the carbon atom pairs [61]. Atomistic simulation study on uniaxial compression and decompression gave a consistent with our research [49]. Models have also been constructed on the basis of high-resolution transmission electron microscopy observations for glassy carbon structures incorporating non-six-membered rings [62], and fragments of the negatively curved graphitic sheets containing linked hexagons with dispersed pentagons and heptagons were distributed randomly throughout

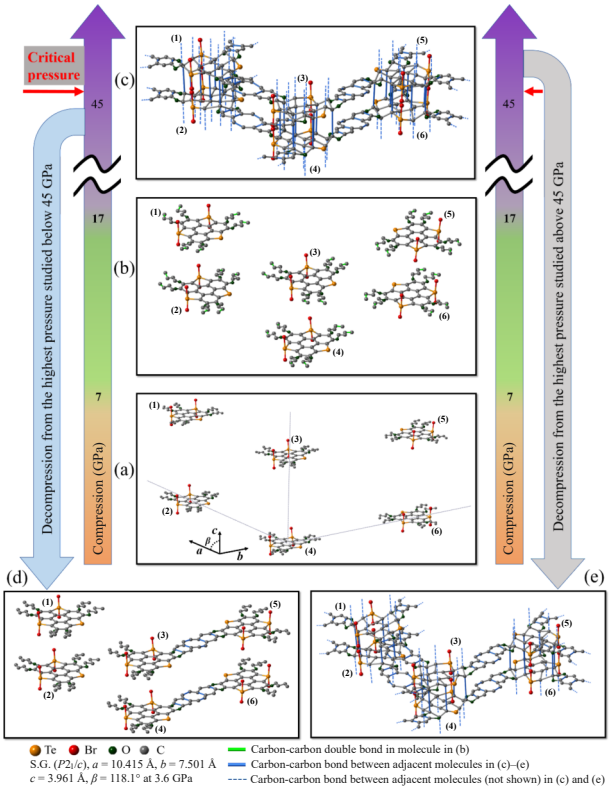

Figure 6 Schematic of $C_{18}Te_3Br_4(Bu\text{-}O)_6$ evolution with high-pressure (hydrogen atoms were omitted for clarity). (a) $C_{18}Te_3Br_4(Bu\text{-}O)_6$ at 3 GPa, (b) $C_{18}Te_3Br_4(3\text{-butenyl-}O)_6$, which formed after $C_{18}Te_3Br_4(Bu\text{-}O)_6$ pressure-induced decomposition, (c) high sp^3 amorphous state above 17.0 GPa after pressure-induced diamondization by means of a "chair" transformation from a structure with ···[AAA]··· stacking to hexagonal diamond, (d) flake clusters after decompression below 45 GPa, and (e) the low sp^3 amorphous state after decompression above 45 GPa.

the network [63]. Another assessment by Martin et al. found that the dipole moments in curved polyaromatic hydrocarbons as a result of pentagonal inclusions produced significant long-range interactions, which contributed to the self-assembly processes [64].

A study by Wentorf et al. showed that the final product from naphthalene, anthracene, and chrysene at 12 GPa and 2,000 °C was graphite, whereas the same treatment of adamantane, camphene, pyrene, fluorene, and polyethylene resulted in diamondization with approximately 60% yield. Therefore, it was assumed that the state of the starting material (including molecular structure and hydrogen-based functional groups) would affect the resulting pyrolysis products under pressure [65]. Research on hydrogenated amorphous carbon and hydrogenated graphitic carbon films irradiated by ions confirmed that the trigonal-bonded carbon and cluster size were dependent on the hydrogen concentration [66]. Several PAHs subjected to high temperature and high-pressure conditions were studied by Davydov et al., and the results showed that specific structures of the initial compounds, especially hydrogen content, played an important role in diamond formation from graphite and carbon residue [17]. Martins et al. performed Raman spectroscopy and found that pressure-induced diamondization on the surface of graphene was facilitated by the hydrogen-based chemical groups [67]. In addition, Gao et al. [68] and Dong et al. [69] disclosed that shear stress played an important role in the conversion of intramolecular sp^2 bonding to intermolecular sp^3 bonding during diamond formation. However, the transition pressure differences between these two studies were 30–50 times. Furthermore, *in situ* Raman spectroscopy analysis showed no noticeable changes in the types of chemical bonds in glassy carbon, up to 60 GPa [70]. Therefore, studies have not yet determined whether hydrogen atoms or shear forces play a major role in the conversion.

Ultraviolet–visible (UV) Raman spectroscopy was used to analyze the linkage of unsaturated benzene under pressure, which produced networks containing both sp^2-bonded and sp^3-bonded carbon structures and the results showed that benzene ring aromaticity must be destroyed during network formation [71]. In addition, two π-systems nonplanar structural elements were found to combine into new polyarene through sp^2 bonding on the edges of the molecules [72]. The polymerization reaction occurred at 10–20 GPa for distance-selected 1,4-diphenylbutadiyne under high-pressure conditions, forming crystalline graphitic nanoribbons [38]. Therefore, the product formed by pressure-induced polymerization through a variety of routes, and a unified criterion for producing specific polymer structures via specific routes is urgently needed.

4 Conclusions

In this study, we used IR absorption spectroscopy, Raman spectroscopy, synchrotron XRD and electrochemical impedance spectroscopy to determine that bowl-shaped $C_{18}Te_3Br_4(Bu\text{-}O)_6$ exhibited a pressure-dependent transport property resulting from structural evolution. Due to pressure-induced DDA reaction at ~ 7 GPa, the saturated sp^3-bonded carbon of the butyl group decomposed to unsaturated sp^2-bonded carbon. Above 17.0 GPa, the sample presented bonding conversion from intramolecular sp^2 in a molecular crystal into intermolecular sp^3 in an amorphous state; thus, pressure-induced diamondization occurred. A carbon network with a high sp^3 amorphous state formed, and a good carrier transmission channel was established, which decreased the resistance for ionic conduction. We also observed a critical pressure at 45 GPa. When the highest pressure applied to the sample was lower than the critical pressure, the conversion from sp^2 bonding to sp^3 bonding was an incomplete reversibility. All C–C bridges and a few of sp^3 bonds of molecular edge broken, so flake cluster consisting of several molecules formed. After pressure unloading from the highest pressure above 45 GPa, we observed decompression-induced graphitization of glassy carbon. All of the sp^3 bonds on the molecular edges and some of intermolecular sp^3 bonds in the rings remained unchanged. Therefore, a low sp^3 amorphous structure formed. Our experimental results showed that pressure could be effectively used to modify the structure and electrical properties of bowl-shaped molecular materials.

Acknowledgements

This work was supported by the National Natural Science Foundation of China (Nos. 52090020 and 11874076) and the National Research Foundation of Korea (Nos. 2016K1A4A3914691 and 2018R1DA1B070498).

Electronic Supplementary Material: Supplementary material (*in situ* synchrotron XRD patterns of Fe from 3.6 to 20.6 GPa) is available in the online version of this article at https://doi.org/10.1007/s12274-022-4215-8.

References

[1] Wang, Z. R.; Yu, F.; Xie, J.; Zhao, J. F.; Zou, Y.; Wang, Z. P.; Zhang, Q. C. Insights into the control of optoelectronic properties in mixed-stacking charge-transfer complexes. *Chem.—Eur. J.* **2020**, *26*, 3578–3585.

[2] Dong, H. L.; Zhu, H. F.; Meng, Q.; Gong, X.; Hu, W. P. Organic photoresponse materials and devices. *Chem. Soc. Rev.* **2012**, *41*, 1754–1808.

[3] Sun, Y. G.; Wang, L.; Liu, Y. Z.; Ren, Y. Birnessite-type MnO_2 nanosheets with layered structures under high pressure: Elimination of crystalline stacking faults and oriented laminar assembly. *Small* **2015**, *11*, 300–305.

[4] Zhang, L. J.; Wang, Y. C.; Lv, J.; Ma, Y. M. Materials discovery at high pressures. *Nat. Rev. Mater.* **2017**, *2*, 17005.

[5] Mao, H. K.; Chen, X. J.; Ding, Y.; Li, B.; Wang, L. Solids, liquids, and gases under high pressure. *Rev. Mod. Phys.* **2018**, *90*, 015007.

[6] Ceppatelli, M.; Santoro, M.; Bini, R.; Schettino, V. High pressure reactivity of solid furan probed by infrared and Raman spectroscopy. *J. Chem. Phys.* **2003**, *118*, 1499–1506.

[7] Sun, J. M.; Dong, X.; Wang, Y. J.; Li, K.; Zheng, H. Y.; Wang, L. J.; Cody, G. D.; Tulk, C. A.; Molaison, J. J.; Lin, X. H. et al. Pressure-induced polymerization of acetylene: Structure-directed stereoselectivity and a possible route to graphane. *Angew. Chem., Int. Ed.* **2017**, *56*, 6553–6557.

[8] Zhao, X. M.; Zhong, G. H.; Zhang, J.; Huang, Q. W.; Goncharov, A. F.; Lin, H. Q.; Chen, X. J. Combined experimental and computational study of high-pressure behavior of triphenylene. *Sci. Rep.* **2016**, *6*, 25600.

[9] Ray, P.; Gray, J. L.; Badding, J. V.; Lueking, A. D. High-pressure reactivity of triptycene probed by Raman spectroscopy. *J. Phys. Chem. B* **2016**, *120*, 11035–11042.

[10] Ciabini, L.; Santoro, M.; Bini, R.; Schettino, V. High pressure reactivity of solid benzene probed by infrared spectroscopy. *J. Chem. Phys.* **2002**, *116*, 2928–2935.

[11] Ke, F.; Chen, Y. B.; Yin, K. T.; Yan, J. J.; Zhang, H. Z.; Liu, Z. X.; Tse, J. S.; Wu, J. Q.; Mao, H. K.; Chen, B. Large bandgap of pressurized trilayer graphene. *Proc. Natl. Acad. Sci. USA* **2019**, *116*, 9186–9190.

[12] Samanta, S.; Lee, M.; Kim, D. S.; Kim, J.; Wang, L. High-pressure triggered quantum tunneling tuning through classical percolation in a single nanowire of a binary composite. *Nano Res.* **2019**, *12*, 1333–1338.

[13] Ciabini, L.; Santoro, M.; Gorelli, F. A.; Bini, R.; Schettino, V.; Raugei, S. Triggering dynamics of the high-pressure benzene amorphization. *Nat. Mater.* **2007**, *6*, 39–43.

[14] Wang, Y. J.; Wang, L. J.; Zheng, H. Y.; Li, K.; Andrzejewski, M.; Hattori, T.; Sano-Furukawa, A.; Katrusiak, A.; Meng, Y. F.; Liao, F. H. et al. Phase transitions and polymerization of C_6H_6–C_6F_6 cocrystal under extreme conditions. *J. Phys. Chem. C* **2016**, *120*, 29510–29519.

[15] Wang, Y. J.; Dong, X.; Tang, X. Y.; Zheng, H. Y.; Li, K.; Lin, X. H.; Fang, L. M.; Sun, G. A.; Chen, X. P.; Xie, L. et al. Pressure-induced Diels–Alder reactions in C_6H_6–C_6F_6 cocrystal towards graphane structure. *Angew. Chem., Int. Ed.* **2019**, *58*, 1468–1473.

[16] Aust, R. B.; Bentley, W. H.; Drickamer, H. G. Behavior of fused-ring aromatic hydrocarbons at very high pressure. *J. Chem. Phys.* **1964**, *41*, 1856–1864.

[17] Davydov, V. A.; Rakhmanina, A. V.; Agafonov, V.; Narymbetov, B.; Boudou, J. P.; Szwarc, H. Conversion of polycyclic aromatic hydrocarbons to graphite and diamond at high pressures. *Carbon* **2004**, *42*, 261–269.

[18] Wang, L.; Liu, B. B.; Li, H.; Yang, W. G.; Ding, Y.; Sinogeikin, S. V.; Meng, Y.; Liu, Z. X.; Zeng, X. C.; Mao, W. L. Long-range ordered carbon clusters: A crystalline material with amorphous building blocks. *Science* **2012**, *337*, 825–828.

[19] Li, B.; Zhang, J. B.; Yan, Z. P.; Feng, M. N.; Yu, Z. H.; Wang, L. Pressure-induced dimerization of C_{60} at room temperature as revealed by an *in situ* spectroscopy study using an infrared laser. *Crystals* **2020**, *10*, 182.

[20] Pei, C. Y.; Feng, M. N.; Yang, Z. X.; Yao, M. G.; Yuan, Y.; Li, X.; Hu, B. W.; Shen, M.; Chen, B.; Sundqvist, B. et al. Quasi 3D polymerization in C_{60} bilayers in a fullerene solvate. *Carbon* **2017**, *124*, 499–505.

[21] Wang, L.; Liu, B.; Liu, D.; Hou, Y.; Yao, M.; Zou, G.; Li, H.; Luo, C.; Li, Y.; Liu, J. High pressure studies of nano/sub-micrometer C_{70} rods. *Chin. Phys. C: High Energy Phys. Nucl. Phys.* **2005**, *29*, 112–115.

[22] Chen, J. Y.; Kim, M.; Yoo, C. S. High structural stability of single wall carbon nanotube under quasi-hydrostatic high pressures. *Chem. Phys. Lett.* **2009**, *479*, 91–94.

[23] Iizumi, Y.; Liu, Z.; Suenaga, K.; Okada, S.; Higashibayashi, S.; Sakurai, H.; Okazaki, T. Molecular arrangements of corannulene and sumanene in single-walled carbon nanotubes. *ChemNanoMat* **2018**, *4*, 557–561.

[24] Okazaki, T.; Iizumi, Y.; Okubo, S.; Kataura, H.; Liu, Z.; Suenaga, K.; Tahara, Y.; Yudasaka, M.; Okada, S.; Iijima, S. Coaxially stacked coronene columns inside single-walled carbon nanotubes. *Angew. Chem., Int. Ed.* **2011**, *50*, 4853–4857.

[25] Alvarez, L.; Le Parc, R.; Jourdain, V.; Dennler, S.; Bantignies, J. L.; Sauvajol, J. L.; Rose, J. A.; Scott, L. T. Temperature dependence and pressure dependence of the vibrational properties of corannulene. *Phys. Status Solidi (B)* **2008**, *245*, 2261–2263.

[26] Du, M. R.; Dong, J. J.; Zhang, Y.; Yang, X. G.; Li, Z. P.; Wang, M. C.; Liu, R.; Liu, B.; Zhou, Q. J.; Wei, T. et al. Vibrational properties and polymerization of corannulene under pressure, probed by Raman and infrared spectroscopies. *J. Phys. Chem. C* **2019**, *123*, 23674–23681.

[27] Hanson, J. C.; Nordman, C. E. The crystal and molecular structure of corannulene, $C_{20}H_{10}$. *Acta Cryst. B* **1976**, *32*, 1147–1153.

[28] Shang, Y. C.; Liu, Z. D.; Dong, J. J.; Yao, M. G.; Yang, Z. X.; Li, Q. J.; Zhai, C. G.; Shen, F. R.; Hou, X. Y.; Wang, L. et al. Ultrahard bulk amorphous carbon from collapsed fullerene. *Nature* **2021**, *599*, 599–604.

[29] Tang, H.; Yuan, X. H.; Cheng, Y.; Fei, H. Z.; Liu, F. Y.; Liang, T.; Zeng, Z. D.; Ishii, T.; Wang, M. S.; Katsura, T. et al. Synthesis of paracrystalline diamond. *Nature* **2021**, *599*, 605–610.

[30] Li, X. X.; Zhu, Y. T.; Shao, J. F.; Wang, B. L.; Zhang, S. X.; Shao, Y. L.; Jin, X. J.; Yao, X. J.; Fang, R.; Shao, X. F. Non-pyrolytic, large-scale synthesis of trichalcogenasumanene: A two-step approach. *Angew. Chem., Int. Ed.* **2014**, *53*, 535–538.

[31] Wang, S. T.; Li, X. X.; Hou, X. Q.; Sun, Y. T.; Shao, X. F. Tritellurasumanene: Ultrasound assisted one-pot synthesis and extended valence adducts with bromine. *Chem. Commun.* **2016**, *52*, 14486–14489.

[32] McCormick, T. M.; Jahnke, A. A.; Lough, A. J.; Seferos, D. S. Tellurophenes with delocalized π-systems and their extended valence adducts. *J. Am. Chem. Soc.* **2012**, *134*, 3542–3548.

[33] Mao, H. K.; Xu, J.; Bell, P. M. Calibration of the ruby pressure gauge to 800 kbar under quasi-hydrostatic conditions. *J. Geophys. Res.:Solid Earth* **1986**, *91*, 4673–4676.

[34] Rahman, S.; Saqib, H.; Zhang, J. B.; Errandonea, D.; Menéndez, C.; Cazorla, C.; Samanta, S.; Li, X. D.; Lu, J. L.; Wang, L. Pressure-induced structural and semiconductor-semiconductor transitions in $Co_{0.5}Mg_{0.5}Cr_2O_4$. *Phys. Rev. B* **2018**, *97*, 174102.

[35] Prescher, C.; Prakapenka, V. B. *DIOPTAS*: A program for reduction of two-dimensional X-ray diffraction data and data exploration. *High Press. Res.* **2015**, *35*, 223–230.

[36] Dischler, B.; Bubenzer, A.; Koidl, P. Bonding in hydrogenated hard carbon studied by optical spectroscopy. *Solid State Commun.* **1983**, *48*, 105–108.

[37] Dischler, B; Bubenzer, A.; Koidl, P. Hard carbon coatings with low optical absorption. *Appl. Phys. Lett.* **1983**, *42*, 636–638.

[38] Zhang, P. J.; Tang, X. Y.; Wang, Y. D.; Wang, X.; Gao, D. X.; Li, Y. P.; Zheng, H. Y.; Wang, Y. J.; Wang, X. X.; Fu, R. Q. et al. Distance-selected topochemical dehydro-Diels–Alder reaction of 1, 4-diphenylbutadiyne toward crystalline graphitic nanoribbons. *J. Am. Chem. Soc.* **2020**, *142*, 17662–17669.

[39] Chanyshev, A. D.; Litasov, K. D.; Shatskiy, A. F.; Ohtani, E. *In situ* X-ray diffraction study of decomposition of polycyclic aromatic hydrocarbons at pressures of 7–15 GPa: Implication to fluids under the Earth's and planetary environments. *Chem. Geol.* **2015**, *405*, 39–47.

[40] Kvashnin, A. G.; Chernozatonskii, L. A.; Yakobson, B. I.; Sorokin, P. B. Phase diagram of quasi-two-dimensional carbon, from graphene to diamond. *Nano Lett.* **2014**, *14*, 676–681.

[41] Mimura, K.; Toyama, S.; Sugitani, K. Shock-induced dehydrogenation of polycyclic aromatic hydrocarbons with or without serpentine: Implications for planetary accretion. *Earth*

Planet. Sci. Lett. **2005**, *232*, 143–156.
[42] Sun, B.; Dreger, Z. A.; Gupta, Y. M. High-pressure effects in pyrene crystals: Vibrational spectroscopy. *J. Phys. Chem. A* **2008**, *112*, 10546–10551.
[43] Schindler, T. L.; Vohra, Y. K. A micro-Raman investigation of high-pressure quenched graphite. *J. Phys.:Condens. Matter* **1996**, *8*, 3963.
[44] Ferrari, A. C.; Robertson, J. Interpretation of Raman spectra of disordered and amorphous carbon. *Phys. Rev. B* **2000**, *61*, 14095–14107.
[45] Goncharov, A. F.; Makarenko, I. N.; Stishov, S. M. Graphite at pressures up to 55 GPa: Optical properties and Raman scattering-amorphous carbon. *Sov. Phys. JETP* **1989**, *69*, 380–381.
[46] Wang, Y. J.; Panzik, J. E.; Kiefer, B.; Lee, K. K. M. Crystal structure of graphite under room-temperature compression and decompression. *Sci. Rep.* **2012**, *2*, 520.
[47] Yao, M. G.; Xiao, J. P.; Fan, X. H.; Liu, R.; Liu, B. B. Transparent, superhard amorphous carbon phase from compressing glassy carbon. *Appl. Phys. Lett.* **2014**, *104*, 021916.
[48] Barboza, A. P. M.; Guimaraes, M. H. D.; Massote, D. V. P.; Campos, L. C.; Neto, N. M. B.; Cancado, L. G.; Lacerda, R. G.; Chacham, H.; Mazzoni, M. S. C.; Neves, B. R. A. Room-temperature compression-induced diamondization of few-layer graphene. *Adv. Mater.* **2011**, *23*, 3014–3017.
[49] Shiell, T. B.; McCulloch, D. G.; McKenzie, D. R.; Field, M. R.; Haberl, B.; Boehler, R.; Cook, B. A.; de Tomas, C.; Suarez-Martinez, I.; Marks, N. A. et al. Graphitization of glassy carbon after compression at room temperature. *Phys. Rev. Lett.* **2018**, *120*, 215701.
[50] Lim, J.; Yoo, C. S. Intercalation of solid hydrogen into graphite under pressures. *Appl. Phys. Lett.* **2016**, *109*, 051905.
[51] Lin, Y.; Zhang, L.; Mao, H. K.; Chow, P.; Xiao, Y. M.; Baldini, M.; Shu, J. F.; Mao, W. L. Amorphous diamond: A high-pressure superhard carbon allotrope. *Phys. Rev. Lett.* **2011**, *107*, 175504.
[52] Clark, S. M.; Jeon, K. J.; Chen, J. Y.; Yoo, C. S. Few-layer graphene under high pressure: Raman and X-ray diffraction studies. *Solid State Commun.* **2013**, *154*, 15–18.
[53] Garbarczyk, J. E.; Wasiucionek, M.; Machowski, P.; Jakubowski, W. Transition from ionic to electronic conduction in silver–vanadate–phosphate glasses. *Solid State Ion.* **1999**, *119*, 9–14.
[54] Tuller, H. L. Ionic conduction in nanocrystalline materials. *Solid State Ion.* **2000**, *131*, 143–157.
[55] Miller, E. D.; Nesting, D. C.; Badding, J. V. Quenchable transparent phase of carbon. *Chem. Mater.* **1997**, *9*, 18–22.
[56] Wu, J. H.; Wang, S. Y.; Lei, Z. W.; Guan, R. N.; Chen, M. Q.; Du, P. W.; Lu, Y. L.; Cao, R. G.; Yang, S. F. Pomegranate-like C_{60}@cobalt/nitrogen-codoped porous carbon for high-performance oxygen reduction reaction and lithium-sulfur battery. *Nano Res.* **2021**, *14*, 2596–2605.
[57] Soler-Piña, F. J.; Hernández-Rentero, C.; Caballero, A.; Morales, J.; Canales-Vázquez, J. Highly graphitized carbon nanosheets with embedded Ni nanocrystals as anode for Li-ion batteries. *Nano Res.* **2020**, *13*, 86–94.
[58] Li, G. C.; Yin, Z. L.; Dai, Y. Q.; You, B. Z.; Guo, H. J.; Wang, Z. X.; Yan, G. C.; Liu, Y.; Wang, J. X. Graphitic nanorings for super-long lifespan lithium-ion capacitors. *Nano Res.* **2020**, *13*, 2909–2916.
[59] Li, H. Y.; Zhang, L. H.; Li, L.; Wu, C. W.; Huo, Y. J.; Chen, Y.; Liu, X. J.; Ke, X. X.; Luo, J.; Van Tendeloo, G. Two-in-one solution using insect wings to produce graphene–graphite films for efficient electrocatalysis. *Nano Res.* **2019**, *12*, 33–39.
[60] Zhao, X. W.; Wu, Y. Z.; Wang, Y. S.; Wu, H. S.; Yang, Y. W.; Wang, Z. P.; Dai, L. X.; Shang, Y. Y.; Cao, A. Y. High-performance Li-ion batteries based on graphene quantum dot wrapped carbon nanotube hybrid anodes. *Nano Res.* **2020**, *13*, 1044–1052.
[61] Mao, W. L.; Mao, H. K.; Eng, P. J.; Trainor, T. P.; Newville, M.; Kao, C. C.; Heinz, D. L.; Shu, J. F.; Meng, Y.; Hemley, R. J. Bonding changes in compressed superhard graphite. *Science* **2003**, *302*, 425–427.
[62] Harris, P. J. F. Fullerene-related structure of commercial glassy carbons. *Philos. Mag.* **2004**, *84*, 3159–3167.
[63] Townsend, S. J.; Lenosky, T. J.; Muller, D. A.; Nichols, C. S.; Elser, V. Negatively curved graphitic sheet model of amorphous carbon. *Phys. Rev. Lett.* **1992**, *69*, 921–924.
[64] Martin, J. W.; Slavchov, R. I.; Yapp, E. K. Y.; Akroyd, J.; Mosbach, S.; Kraft, M. The polarization of polycyclic aromatic hydrocarbons curved by pentagon incorporation: The role of the flexoelectric dipole. *J. Phys. Chem. C* **2017**, *121*, 27154–27163.
[65] Wentorf, R. H. Jr. The behavior of some carbonaceous materials at very high pressures and high temperatures. *J. Phys. Chem.* **1965**, *69*, 3063–3069.
[66] Compagnini, G.; Calcagno, L.; Foti, G. Hydrogen effect on atomic configuration of keV-ion-irradiated carbon. *Phys. Rev. Lett.* **1992**, *69*, 454–457.
[67] Martins, L. G. P.; Matos, M. J. S.; Paschoal, A. R.; Freire, P. T. C.; Andrade, N. F.; Aguiar, A. L.; Kong, J.; Neves, B. R. A.; de Oliveira, A. B.; Mazzoni, M. S. C. et al. Raman evidence for pressure-induced formation of diamondene. *Nat. Commun.* **2017**, *8*, 96.
[68] Gao, Y.; Ma, Y. Z.; An, Q.; Levitas, V.; Zhang, Y. Y.; Feng, B.; Chaudhuri, J.; Goddard III, W. A. Shear driven formation of nano-diamonds at sub-gigapascals and 300 K. *Carbon* **2019**, *146*, 364–368.
[69] Dong, J. J.; Yao, Z.; Yao, M. G.; Li, R.; Hu, K.; Zhu, L. Y.; Wang, Y.; Sun, H. H.; Sundqvist, B.; Yang, K. et al. Decompression-induced diamond formation from graphite sheared under pressure. *Phys. Rev. Lett.* **2020**, *124*, 065701.
[70] Solopova, N. A.; Dubrovinskaia, N.; Dubrovinsky, L. Raman spectroscopy of glassy carbon up to 60 GPa. *Appl. Phys. Lett.* **2013**, *102*, 121909.
[71] Jackson, B. R.; Trout, C. C.; Badding, J. V. UV Raman analysis of the C: H network formed by compression of benzene. *Chem. Mater.* **2003**, *15*, 1820–1824.
[72] Fujikawa, T.; Preda, D. V.; Segawa, Y.; Itami, K.; Scott, L. T. Corannulene-helicene hybrids: Chiral π-systems comprising both bowl and helical motifs. *Org. Lett.* **2016**, *18*, 3992–3995.